Molecular-dynamics study of ablation of solids under femtosecond laser pulses

Danny Perez* and Laurent J. Lewis†

Département de Physique et Groupe de Recherche en Physique et Technologie des Couches Minces (GCM), Université de Montréal, C. P. 6128 Succursale Centre-Ville, Montréal (Québec), Canada H3C 3J7

(Received 30 October 2002; revised manuscript received 16 January 2003; published 5 May 2003)

The ablation of solids under femtosecond laser pulses is studied using a two-dimensional molecular-dynamics model. The simulations show that different expansion regimes develop as a function of the injected energy. The origin of these regimes lies in changes of the thermodynamical relaxation path the material follows when the intensity of the laser increases. The shape of the pressure waves generated as a result of the absorption of the pulse is shown to vary from bipolar at low fluence to unipolar at high fluence, as a result of the decrease of the tensile strength of the material with temperature. By combining these results with an analysis of the thermodynamical trajectories for different portions of the target, we show that four different mechanisms can account for ablation at fluences below the threshold for plasma formation, namely spallation, phase explosion, fragmentation, and vaporization. These mechanisms are characterized in detail; it is demonstrated that they can occur simultaneously in different parts of the target.

DOI: 10.1103/PhysRevB.67.184102 PACS number(s): 79.20.Ds, 79.20.Ap, 61.80.Az

I. INTRODUCTION

The ablation of matter from a target induced by laser pulses is a well-known technique routinely used in a number of areas. It is now appreciated that very short (femtosecond) pulses offer numerous advantages over longer pulses: the high efficiency (yield/injected energy) and the small thermal and mechanical damages inflicted to the target are invaluable characteristics for, e.g., micromachining[1,2] and biomedical applications.[2–4] Femtosecond laser pulses are also ideal for studying the fundamental properties of matter in extreme conditions of temperature and pressure.[5,6]

However, the basic mechanisms leading to ablation are poorly understood, largely because theoretical modeling of laser ablation is difficult. Indeed, many processes are induced by the absorption of high quantities of energy in very short times. On a microscopic scale, these include: dielectric breakdown in transparent solids,[7] change of optical and electronic properties,[8] nonthermal melting of covalent materials,[9] and semiconductor-to-metal transitions.[10] On a mesoscopic scale, the pressure wave generation,[3,11,12] the thermodynamical evolution of the expanding matter,[5,13] and the identification of the collective ejection processes[5,14–21] must all be understood in order to provide a complete picture of the phenomenon.

While a complete, microscopic description of femtosecond ablation is out of reach of present models, progress made in the study of the mechanisms leading to ablation can nevertheless have significant impacts on applications. Many mechanisms are believed to play a role in ablation below the threshold for plasma formation: photomechanical spallation (in organic solids),[3,19] homogeneous nucleation of gas bubbles and phase explosion,[5,14–16,19,21] spinodal decomposition,[5,20] fragmentation,[21] and vaporization.[17]

Here we study the mesoscopic aspects of laser ablation using a simple two-dimensional molecular dynamics model. Because they determine the conditions in which ablation occurs, the expansion dynamics of the irradiated target and the generation of pressures waves will first be investigated. It will be shown that different expansion regimes appear as a function of the injected energy (and hence depth under the surface). The origin of these regimes is traced back to variations in the thermodynamical relaxation path followed by the expanding matter as the injected energy increases. It will also be shown that these regimes explain the formation (at low fluence) and disappearance (at high fluence) of the optical interference patterns observed in experiments (Newton rings).[5] Pressure waves generated during the relaxation process also suffer some changes as the fluence is increased: the profile transforms from bipolar at low fluence to unipolar at high fluence because of the loss of tensile resistance of the material (thermal softening) at high temperature. Following the preliminary results presented in Ref. 21, we show that knowledge of the precise thermodynamical evolution of the target, not easily accessible to experiment, is the key to the identification of the ablation process. Spallation, homogeneous nucleation, fragmentation, and vaporization are shown to be relevant to the description of ablation in the femtosecond regime, and can occur simultaneously in different regions of the target. Furthermore, the occurrence of these ablation mechanisms are related to the mechanical and thermodynamical properties of the material. Finally, the dependence of the ablation depth on fluence is investigated.

The model, the method for calculating thermodynamical trajectories, and the phase diagram of the potential are first presented Sec. II. The overall reaction of the target to the laser-induced heating is discussed in Sec. III A in terms of three aspects: analysis of snapshots of the model system during the ablation process and investigation of the expansion dynamics and of the generation of pressure waves. Identification and discussion of the different ablation processes is presented in Sec. III B. Finally, the variation of the ablation depth with fluence is examined in Sec. III C before concluding.

II. COMPUTATIONAL METHODS

A. Model

We study the ablation process using molecular-dynamics simulations[22] in two dimensions, thereby enabling large sys-

tems to be considered, thus minimizing finite-size effects, which could be a problem in the case of homogeneous nucleation, as the system has to be able to accommodate many critical nuclei. Anticipating the results, our analysis shows that the nature of the ablation process depends essentially on the thermodynamic pathways by which the system relaxes. Since the phase diagram of our two-dimensional system is qualitatively the same as its three-dimensional counterpart, there is no reason to expect the nature of the mechanisms of ablation to depend in a significant manner on dimensionality, even if the precise kinetics of the ablation process will probably be somewhat affected.

Simulations were carried out using samples with either 400 or 800 atomic layers in the y direction (parallel to the incident laser pulse) and 500 layers in the x direction, for a total of 200 000 or 400 000 atoms initially forming a triangular lattice. The lattice was thermalized in the low temperature solid state before beginning the simulations. The atoms interact via a simple Lennard-Jones potential adjusted so as to vanish at the cutoff distance r_c:

$$\phi_{\mathrm{LJ}}(r)=4\epsilon[(\sigma/r)^{12}-(\sigma/r)^{6}-(\sigma/r_c)^{12}+(\sigma/r_c)^{6}],\quad r\leqslant r_c,$$

$$\phi_{\mathrm{LJ}}(r)=0,\quad r>r_c$$

with ϵ and σ the usual energy and length scales, respectively. We used $r_c=2.5\sigma$. In the following, all results are reported in reduced units, i.e., ϵ/k_B for temperature and $\tau=(m\sigma^2/\epsilon)^{1/2}$ for time (m is the atomic mass). This potential was chosen for its simplicity and because it captures the essential features of realistic interatomic potentials.

The laser pulse, incident on the target from the y direction, is uniform in space and has a Gaussian temporal profile with a width at half maximum of $\Delta t=0.5\tau$ ($\sim$100 fs). The pulse is modeled as an ensemble of discrete photons of energy 4.5ϵ, emitted using appropriate distributions. The energy absorption inside the target follows a Beer-Lambert law ($I=I_0e^{-\alpha y}$) where α is the absorption coefficient; two values were examined: $\alpha=0.01$ or $0.002\sigma^{-1}$ ($[\simeq 20$ or $\simeq 100$ nm$]^{-1}$). Absorption of the photons by the target proceeds by the transfer of its energy to a ''carrier.'' Here, a carrier is a particle which follows a Drude dynamics, i.e., the dynamics is governed by successive collisions determined by a characteristic scattering time taken to be 0.005τ. At each collision, a ''phonon'' of energy 0.07ϵ ($\sim$50 meV) is transferred from the carrier to the nearest atom if the carrier possesses sufficient energy. This is accomplished by adding an appropriate component to the velocity of the atom in a random direction. The carriers cannot absorb energy from the target. It must be stressed that it is not our goal to mimic realistic carrier dynamics, but only to model in a physically relevant manner the rate at which the energy is deposited.

The rapid heating of the target following the absorption of light generates important pressure waves that must be dealt with in a proper way to avoid artifacts in the simulations. In order to do this, we use the absorbing boundary conditions proposed in Ref. 23 in the y direction; periodic boundary conditions are used in the x direction. A Langevin heat bath is also used at the bottom of the target in order to mimic heat diffusion outside of the simulation cell.

As stated earlier, this simple model is not meant to reproduce light-matter interactions in a rigorous way. In fact, this is not essential: for fluences close to the ablation threshold, thermal equilibrium is achieved in a few picoseconds while ablation occurs hundreds of picoseconds later.[24] The details of the energy deposition process are thus ''forgotten'' by the time ablation occurs. We expect that, except in specific cases such as nonthermal melting of covalent materials, the details of the ultrafast dynamics of the laser-excited carriers will not influence the *nature* of the ablation process so that our simplified model is adequate.

B. Calculation of local thermodynamical properties

The analysis which follows relies heavily on local, phase-specific thermodynamical properties of small sections of the system. In particular, we are interested in groups of atoms that have absorbed similar quantities of energy so as to determine their common thermodynamical evolution. Care is needed in computing this; the method used to do so is described here.

The target is separated into ''slices'' perpendicular to the incident light; we chose them to be four-layer thick. This grouping is preserved during the whole simulation; however, only the N atoms lying within one standard deviation of the mean y position of the atoms in the slice are taken as representative and used to compute the local thermodynamical quantities ρ, P and T as a function of time. This procedure minimizes the effect of mixing between adjacent layers on the computation of the thermodynamic trajectories. The temperature and pressure are obtained using the standard formulas

$$T=\frac{m}{2N}\sum_{i=1}^{N}(v_i-v_{cm})^2 \tag{1}$$

and

$$P=A^{-1}(\mathcal{W}+NT), \tag{2}$$

where v_{cm} is the center-of-mass velocity of the slice, A the area occupied by the slice, and $\mathcal{W}$ the virial sum. The area occupied by such small subsystems is most difficult to obtain (and even to define). To circumvent this difficulty, a tessellation of space into Voronoi polygons centered around atomic positions is used, as shown in Fig. 1. The area occupied by a group of atoms is defined as the sum of the areas of their respective polygons. This procedure is free from arbitrary parameters. The trajectories obtained in this way will be referred to as average, as they give a macroscopic view of the system, independent of the presence of pores or clusters.

Inhomogeneities can (and will) develop during the ablation process; therefore it is desirable to follow the evolution of the clusters and of the gas separately using a condensed and a gas branch. In order to do this, clustered and isolated atoms are first identified using the Hoshen-Kopelman algorithm.[25] The clustering radius is chosen so that the critical point density separates the gas and condensed regions.

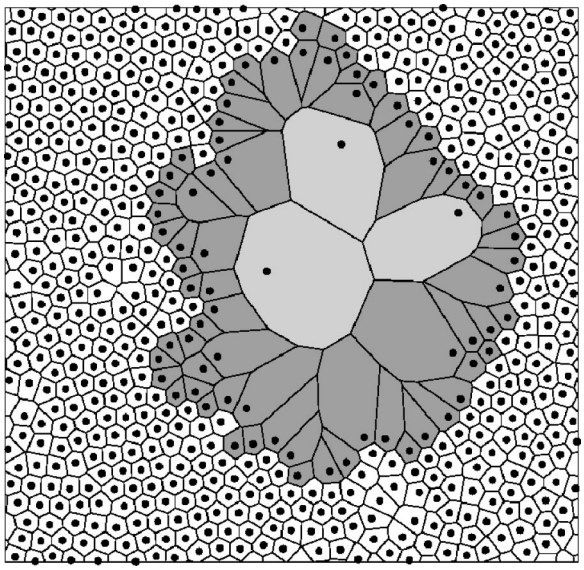

FIG. 1. Phase-specific density calculation. White: condensed bulk atoms; dark gray: condensed surface atoms; light gray: isolated atoms.

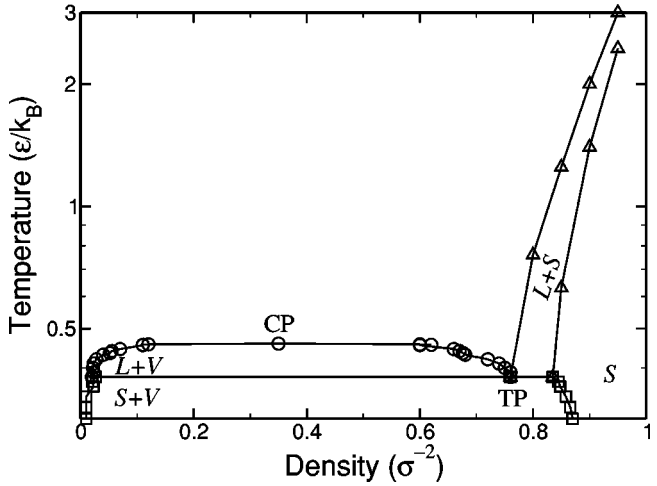

FIG. 2. Phase diagram of the 2D truncated and shifted Lennard-Jones potential in the ρ-T plane. Circles: binodal line (liquid-vapor coexistence); squares: solid-vapor coexistence line; triangles: solid-liquid coexistence line. The solid line is drawn to guide the eye. The italic letters refer the the phases in each regions (S,L,V: solid, liquid, and vapor, respectively). CP: critical point, TP: triple point.

The condensed (clustered) atoms are then separated into two categories: bulk (fully coordinated) and surface (undercoordinated) (see Fig. 1). The area occupied by the condense phase is defined as the total number of clustered atoms times the mean area of the Voronoi polygons for atoms in the bulk subgroup. The difference between the total area of the slice and the area occupied by the condense phase is attributed to the gas phase. In this way, the area of the large Voronoi polygons of surface atoms is mostly attributed to the gas phase. With this procedure, it is possible to obtain phase-specific thermodynamical quantities using Eqs. (1) and (2) by averaging over the appropriate subgroup of atoms. For the temperature on the condensed branch, different v_{cm}'s are used for each cluster.

As will be shown in Sec. III B, the use of these three different thermodynamical trajectories (average, condensed, and gas) allows the type of process responsible for the ablation of a particular slice to be identified, because a correlation between the formation of voids inside the target (which causes the average and condensed branches to split) and the instantaneous thermodynamical state of the system can be established.

C. Phase diagram of the two-dimensional truncated and shifted LJ system

In order for the thermodynamical trajectory calculations to be useful, the phase diagram of our model system must be known. Because the phase diagram is very sensitive to small modifications of the potential (such as truncation and shifting), the abundant data published for the full LJ potential cannot be employed here and calculations had to be performed in order to complete the data available for the particular version of the LJ potential we use. The phase diagram we obtained is presented in Fig. 2. The binodal (liquid-vapor coexistence) line was partially taken from Ref. 26 and completed down to the triple point using Gibbs ensemble Monte Carlo simulations.[27] The solid-vapor coexistence region was also obtained using this method. Because the Gibbs ensemble Monte Carlo method does not work well at high density, the position of the solid-liquid coexistence region was inferred from the temperature change of the entropy, which was computed with the method of Ref. 28. The isentropes obtained in this way were also used to obtain the speed of sound inside the LJ system as a function of temperature and density $[c^2=(\partial P/\partial\rho)_S]$.

III. RESULTS

A. Reaction of the target after the absorption of a pulse

We first discuss the global reaction of the system after the absorption of the pulse. This analysis develops along three lines. First, using snapshots from the simulations, we show that different morphological and dynamical features are observed in the target depending on the energy density locally absorbed. Second, the expansion dynamics is discussed and the origin of the different regimes is linked to changes in the thermodynamical relaxation paths of the material. We also confirm the model proposed by Sokolowski-Tinten *et al.*[5] to explain the formation of optical interference patterns during ablation. Third, and last, variations of the characteristics of the acoustic waves generated by the relaxation of the thermoelastic pressure distribution induced by the laser heating are analyzed and related to the mechanical properties of the material.

1. Visual analysis

Figures 3 and 4 show snapshots the of simulations for the system with 400 000 atoms and a small absorption coefficient ($\alpha=0.002\sigma^{-1}$) at different moments during the simulation. The evolution of the system at low fluence (F

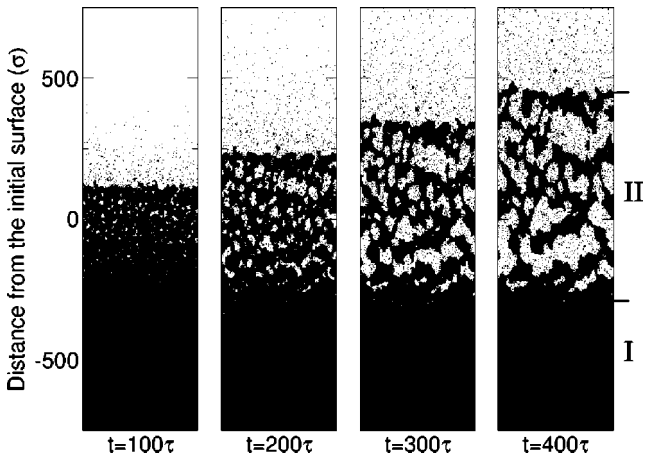

FIG. 3. Snapshots of a simulation with $F=900\epsilon/\sigma=1.2F_{\mathrm{th}}$ and $\alpha=0.002\sigma^{-1}$. Roman numerals identify different regions of the target (see text).

$=1.2F_{\mathrm{th}}$, where F_{th} is the threshold fluence for ablation) is discussed first in Fig. 3. The laser pulse is fired during the first 2τ. In spite of the drastic heating which occurs during the relaxation of the carrier gas, the target does not react before about $t=5\tau$. At this moment, the important pressure build-up generated by the isochoric heating is relaxed by the emission of a pressure wave (see later) and the expansion of the target starts. Emission of monomers from the surface has also begun by then. At around $t=100\tau$ (first snapshot), nucleation of small pores is initiated in the surface region. At $t=200\tau$, it is apparent that these voids are filled with gas. During the next 200τ, intense growth and coalescence occur so that the size of the voids increases rapidly. This finally leads to the ablation of large liquid droplets from the topmost 300σ of the target. An interesting feature of the plume in this case is that the matter-vacuum interface progresses slowly and stays relatively sharp for a long period of time. We will show later that this can explain the observation of optical interference patterns in short-pulse laser ablation experiments.[5] Despite the exponential temperature profile initially imposed by the laser pulse, the reaction of the system is remarkably homogeneous: the size of pores and their gas content do not seem to depend strongly on the depth below the surface. In this case only two regions are distinguishable: the non-ablated solid region and the porous region, numbered I and II, respectively.

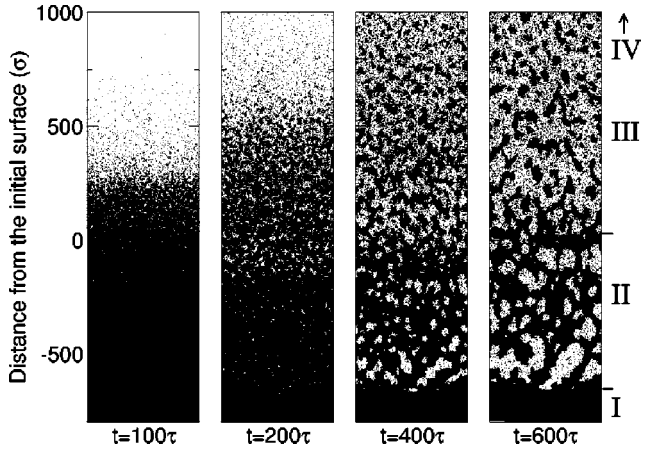

FIG. 4. Snapshots of a simulation with $F=2100\epsilon/\sigma=2.8F_{\mathrm{th}}$ and $\alpha=0.002\sigma^{-1}$. Roman numerals identify different regions of the target. Region IV is the gaseous region (out of the range of the last snapshot).

Figure 4 shows that the situation is somewhat more complex at higher fluence ($F=2.8F_{\mathrm{th}}$). We see from the first snapshot ($t=100\tau$) that expansion and emission of monomers from the surface is now much more intense than in the previous case. Again, small voids are present near the surface at this moment. However, by $t=200\tau$, the coalescence of these voids causes the fast-expanding surface region to decompose into an ensemble of small clusters. Evaporation from the surface of the clusters quickly fills the surrounding area with gas. By then, the front matter-vacuum interface is already destroyed, i.e., the density now varies continuously with position. At $t=400\tau$, many gas-filled pores develop in the bottom section of the target; the morphology of this section is very much like the surface region of Fig. 3. Finally, at $t=600\tau$, the pores coalesce and induce the ejection of this part of the target. At this moment, the cluster creation process in the top part of the target is completed. Now four region are present: the nonablated solid region I, the porous region II, the cluster-filled region III, and a purely gaseous region IV (out of the range of the last snapshot). By comparing the snapshots, we see that each region expands at a different velocity: as it does at low fluence, region II expands slowly compared to regions III and IV. The strongly varying morphologies and expansion speeds of the different regions suggest that the ablation mechanisms might be specific to the energy density absorbed, so that many mechanisms may be effective simultaneously at different depths. It will be shown in Sec. III B that this is indeed the case. First, however, we study the origin of these different expansion regimes. This is required in order to understand the conditions in which ablation occurs.

2. Expansion dynamics

The expansion speed profile for the simulation presented in Fig. 4 is shown in Fig. 5. The data is plotted against the effective energy density (E_{eff}), defined as the total energy density injected by the laser minus the energy drained during the formation of the pressure waves. E_{eff} thus represent the *thermal* energy initially stored at different points in the target. The speeds presented in Fig. 5 were obtained by averaging over the quasisteady velocity profile that establishes soon after the passage of the pressure wave. The different expansion regimes are visible in this figure; it will be shown below that each regime is associated with a specific type of thermodynamic relaxation path. In region I (unablated solid) the expansion proceeds at very low speed. A sudden increase in the expansion speed at $E_{\mathrm{eff}}=1.0\epsilon/\sigma^2$ marks the onset of region II, where the expansion speed depends weakly on E_{eff}. This behavior changes again around $E_{\mathrm{eff}}=2.25\epsilon/\sigma^2$, where region III begins. From this point on, the expansion speed increases with E_{eff} at a much larger rate. Finally, in

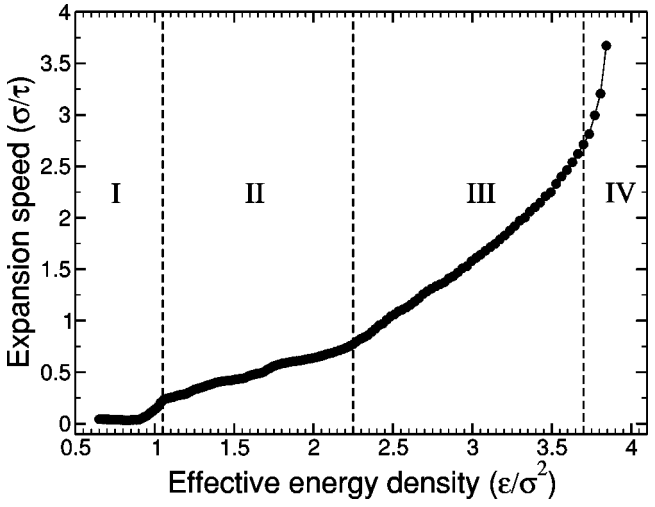

FIG. 5. Expansion speed versus effective energy density for a simulation with $F=2100\ \epsilon/\sigma=2.8F_{\mathrm{th}}$ and $\alpha=0.002\sigma^{-1}$. Roman numerals refer to the regions of the target identified in Figs. 3 and 4.

region IV, the expansion proceeds at a very high speed, typical of the free expansion of a gas.

Because the expansion is mainly driven by the relaxation of the thermoelastic pressure formed during the heating, higher energies will naturally imply higher pressures and hence higher expansion speeds. However, since the induced thermoelastic pressure increases linearly with the injected energy,[18] the formation of distinct expansion regimes cannot be totally explained using a simple pressure relaxation argument. It will now be shown that the origin of these different regimes lies in the change of the thermodynamical relaxation paths as the injected energy increases.

Indeed, Fig. 6 reveals that each expansion regime is associated with a precise type of thermodynamical trajectory. The average trajectories in this figure are typical of slices found inside regions I to IV. In region I, the relaxation (following the constant volume heating of the target) proceeds totally

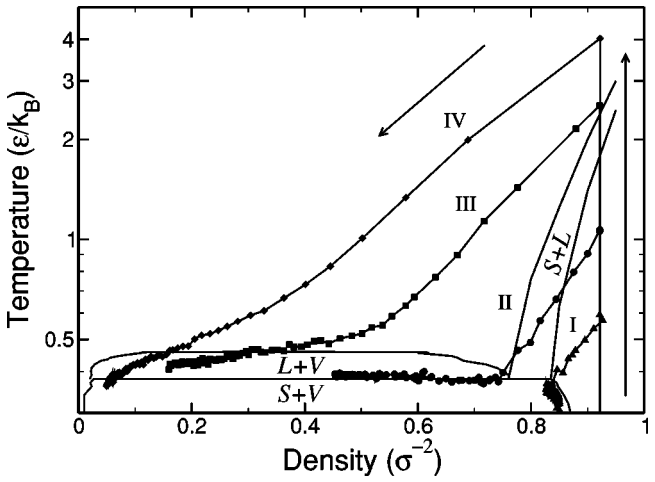

FIG. 6. Examples of average thermodynamical trajectories in different regions of the target, projected in the ρ-T plane. Roman numerals refer to the regions of the target identified in Figs. 3 and 4. Arrows indicate the flow of time.

within the solid region of the phase diagram (see Fig. 2). As this region is not ablated, the final density remains high. The onset of region II is linked to an important change in the thermodynamical trajectory: the target now melts during relaxation. The sudden increase in the expansion speed around $E_{\mathrm{eff}}=1.0\epsilon/\sigma^2$ is thus caused by the abrupt change of volume during the phase transition. Inspection of the samples confirms that this value of E_{eff} indeed marks the boundary between the liquid and solid regions of the target. Further, all trajectories in this region also cross the binodal line between the triple point and the critical point. After crossing the coexistence line, the relaxation continues quasi-isothermally within the liquid-vapor metastable region.

Another important change marks the beginning of region III: the transition from subcritical to supercritical relaxation. Note that, in this case, the late part of the relaxation is no longer isothermal. Finally, in region IV, the relaxation occurs along perfect-gas-like isentropes ($T\propto\rho^{2/3}$), consistent with the diluted-gas nature of the slices during expansion in this region (see Fig. 4).

The relation between the expansion speed and the thermodynamical relaxation path can be studied within a simplified scenario. Consider a semi-infinite homogeneously heated layer initially at uniform density ρ_i. The adiabatic expansion of the material into the vacuum can be described by a self-similar rarefaction wave (SSRW),[29,30] whereby the expansion at density ρ_f proceeds at speed:

$$u(\rho_f,S)=\int_{\rho_i}^{\rho_f}\left(\frac{c(\rho)}{\rho}\right)_S d\rho=\int_{\rho_i}^{\rho_f}\left(\frac{\partial P}{\partial\rho}\right)_S^{1/2}\frac{d\rho}{\rho}, \qquad (3)$$

with $c(\rho)$ the speed of sound and S the entropy The rarefaction (density-decrease) wave is said to be self-similar because the density profile depends solely on a similarity variable $\xi=y/t$, i.e., the dynamics are obtained by simply rescaling the $t=0$ profile. Equation (3) shows that the shape of the isentropes followed during relaxation is crucial for the dynamics of the expansion: flat isentropes (in the ρ-P plane), cause the expansion to proceed slowly while important pressure variations along the isentrope cause a rapid expansion. $u(\rho_f,S)$ was computed along several isentrope (obtained with the method of Ref. 28) and the results are shown in Fig. 7.

A striking feature of these results is the formation of two expansion speed plateaus at low entropy. It was shown by Anisimov *et al.*[30] that this phenomenon occurs because, in the solid-vapor and liquid-vapor coexistence regions, the speed of sound drops sharply, so that $u(\rho_f,S)$ is practically independent of ρ_f below a certain density [see Eq. (3)]. However, as the entropy increases to supercritical values, the abrupt decrease of the speed of sound does not occur anymore and the resulting expansion speeds can take very high values. Note that the variation of the expansion speed with entropy is also very large in the latter case.

While Eq. (3) is strictly valid only in the homogeneous heating limit [$\alpha\rightarrow 0$, i.e., only one $u(\rho_f,S)$ curve is followed during the expansion], the qualitative behavior it predicts gives important physical insights into the more complex expansion dynamics for finite α. In fact, there is a one-

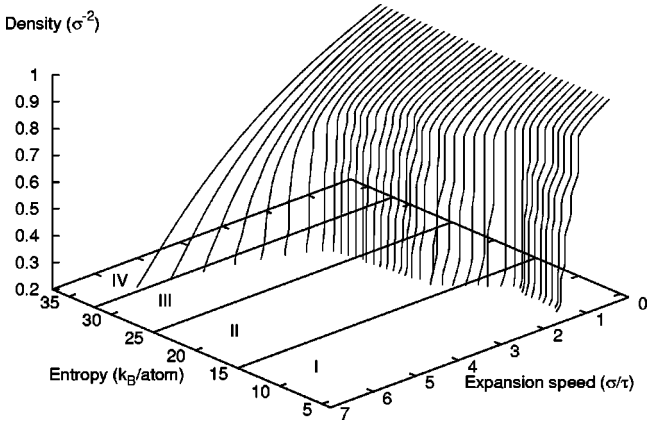

FIG. 7. Density dependence of the expansion speed u as a function of entropy and density for a self-similar rarefaction wave with $\rho_i = 0.92\sigma^{-2}$. Roman numerals refer to the regions of the target identified in Figs. 3 and 4.

to-one correspondence between the regimes observed in the SSRW model and those identified in Fig. 5. First, both Figs. 5 and 7 show two low-speed, weakly entropy-dependent expansion regimes at low entropy (regions I and II) and an increase in du/dE_{eff} as the expansion becomes supercritical (regions III and IV). Second, these regimes occur for the same entropy ranges in the SSRW model that in the finite α case. The connection between the entropy and the effective energy density is obtained through the comparison of different thermodynamical trajectories (and hence effective energy densities) with the isentropes we computed. The qualitative behavior of the expansion speed at finite α thus locally follows that predicted in the SSRW limit: variations of the expansion speed are clearly caused by significant changes in the shape of the thermodynamical relaxation paths as the effective energy (and hence entropy) increases. We will see later that the presence of these different regimes have important consequences for the ablation process.

It can be shown[30] that the density profile $[\rho(y,t)]$ for expansion along a single isentrope in the SSRW model is given by the solution of

$$\xi = \int_{\rho_i}^{\rho} \left(\frac{c(\rho)}{\rho} \right)_S d\rho - c(\rho,S) = u(\rho,S) - c(\rho,S). \qquad (4)$$

Because in the present case the heating profiles are not constant but exponentially decreasing, the SSRW model cannot be used to predict the evolution of the density during the whole expansion process. However, as can be seen from Fig. 7, $u(\rho,S)$ [and hence $c(\rho,S)$] is nearly independent of S in the range $15 < S < 25\ k_B$/atom (region II). The density profile should therefore follow the SSRW prediction as long as the wave runs through regions within this entropy range.

A comparison is carried out in Fig. 8 where the SSRW profile and the simulations results for the target of Fig. 3 are presented. The two indeed agree closely during the early stages of the expansion. The self-similar nature of the wave is destroyed at later time when the wave propagates further into the target, i.e., into region I.

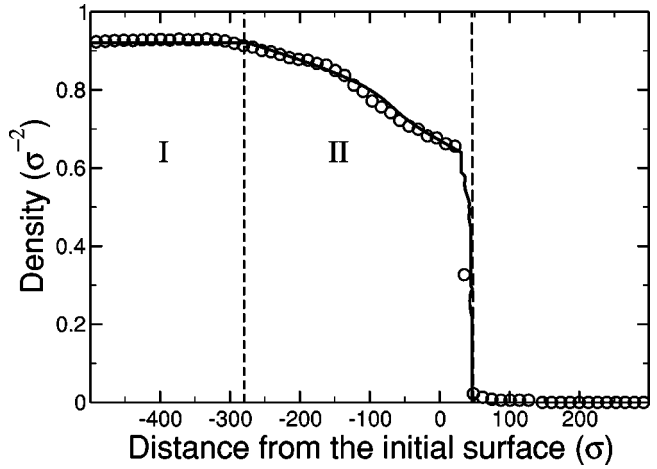

FIG. 8. Density profile at $t = 40\tau$ for $F = 900\ \epsilon/\sigma$ and $\alpha = 0.002\sigma^{-1}$. Full line: self-similar rarefaction wave profile; circles: measured profile. Roman numerals refer to the regions of the target identified in Figs. 3 and 4.

Figure 8 also shows that, as demonstrated in Ref. 30, the SSRW density profile exhibits a very sharp matter-vacuum interface when expansion proceeds through the liquid-vapor coexistence region (e.g., region II). Sokolowski-Tinten *et al.*[5] suggested that a second sharp density discontinuity would form as the rarefaction wave reaches the boundary of the solid, unablated material. If this is the case, the two discontinuities would serve as optical interfaces and hence explain the observation of interference patterns (Newton rings) during short-pulse laser ablation experiments.[5]

Figure 9(a) shows that this interpretation is correct. This figure presents the density profiles of the target of Fig. 3 at different times through the simulation. Here, the expansion proceeds along isentropes which cross the binodal line at the right of the critical point (region II extends up to the surface of the target). The first profile ($t = 40\tau$) corresponds to that of Fig. 8. At $t = 100\tau$, the matter at the tail of the wave —

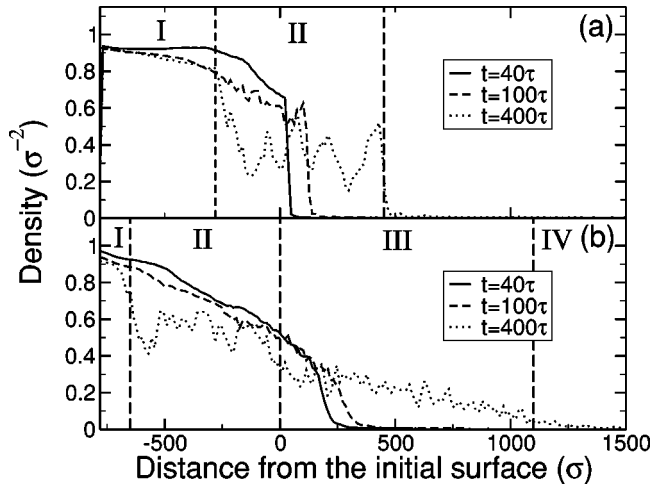

FIG. 9. Density profile at different times for $\alpha = 0.002\sigma^{-1}$: (a) $F = 900\epsilon/\sigma$ and (b) $F = 2100\epsilon/\sigma$. The roman numerals show the extent of the regions of the target identified in Figs. 3 and 4 at $t = 400\tau$.

the matter-vacuum interface — enters the liquid-vapor metastable region and the nucleation of gas bubbles begins. At this same time, the rarefaction wave reaches the boundary of the nonablating region and the self-similar character of the flow is lost. At this moment, the expansion speed difference between the unablated region I and the expanding region II (see Figs. 5 and 7) causes the formation of a second density discontinuity. This discontinuity is fully formed at $t=400\tau$. The figure also shows that the matter-vacuum interface remains sharp during the expansion, even after the self-similar character of the wave is lost. (Note that the interfaces need to be sharp only relative to the probe-light wavelength, typically a few hundred σ, and that the density oscillations in region II are to a large extent caused by statistical fluctuations arising from the finite size of the sample.)

The inhomogeneous phase (region II of Fig. 3) trapped between the two interfaces is thought to possess the optical properties — high refraction index and low absorption coefficient — required to explain the observation of high-contrast interference patterns under normal-incidence optical microscopy.[5] As the thickness of the inhomogeneous layer is comparable to typical laser wavelengths, optical interference can indeed occur. Further, the two interfaces are still sharp by $t=400\tau$, so many more rings should form before the interference condition disappears. Our simulations therefore confirm the mechanisms proposed by Sokolowski-Tinten *et al.*[5] to explain the formation of Newton rings.

However, it is evident from Fig. 4 that the matter-vacuum interface can no longer be sustained when the fluence increases to a point where relaxation occurs along supercritical isentropes, i.e., in regions III and IV. Figure 9(b) shows the changes of the density profile in this case. The evolution is now much more rapid: the rarefaction wave moves quickly and the ablation front is already blunt by $t=40\tau$. At $t=400\tau$ the front interface is totally lost so that the density drops continuously from the bulk value to the vacuum. The strong dependence of the expansion speed on energy in this region is responsible for the destruction of the matter-vacuum interface. This effect is predicted by the SSRW model: for a sharp front to form, the expansion speed of the material is required to depend only weakly on the density over a wide density range.[30] Since this is not the case for supercritical isentropes, the SSRW density profile shows a gradual decrease. As a result, interference patterns are not expected to form under these conditions. The disappearance of Newton rings at high fluence is indeed observed experimentally;[31] our simulations clearly establish that the onset of supercritical expansion in the surface region of the target is responsible for this behavior.

To summarize this section, we have shown that the expansion dynamics of the plume is closely related to the thermodynamical relaxation path along which the material evolves. For relaxation through the solid or the liquid-vapor metastable region, the expansion speed is small and weakly dependent on the isentrope on which expansion proceeds. In contrast, high-speed, strongly energy-dependent expansion occurs for large injected energies. These results are in qualitative agreement with the predicted dependence of the expansion speed on the entropy in the SSRW limit, and are consistent with the formation of Newton rings at low fluence and their disappearance at high fluence, as observed experimentally.

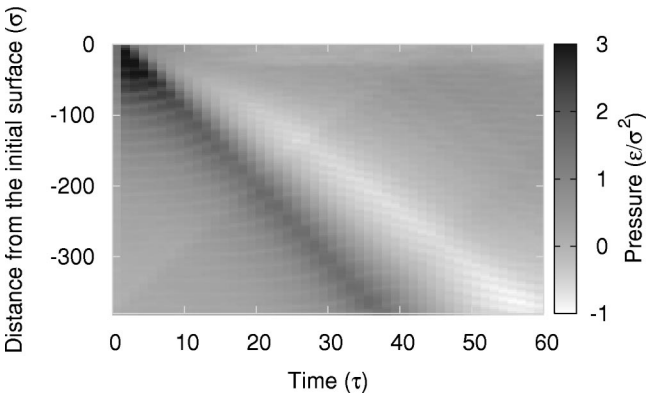

FIG. 10. Pressure in the target as a function of time and position; $F=90\epsilon/\sigma$, $\alpha=0.01\sigma^{-1}$.

3. Pressure wave generation

In the previous section, we have shown that the primary reaction of the system to the absorption of the pulse is to expand in order to relieve the important thermoelastic pressure build-up induced by the constant-volume heating of the target. However, the material also relaxes by emitting strong pressure waves. It has been suggested that these waves could play an important role in the ablation process;[3,4,18,19,32] we now discuss their properties and examine how their shape changes as the fluence increases. It will be shown that a tensile component forms at low fluences but practically disappears as fluence is increased because of the thermal softening of the material in the surface region. Thus, tensile-wave-mediated effects (such as spallation) should be observed only at low fluences.

Relaxation of the thermoelastic stress occurs initially by the emission of two compressive pressure waves: one heading toward the free surface and the other toward the bulk.[11,12,19] The wave incident on the free surface is reflected back and becomes tensile (negative pressure). The tensile component, however, does not fully form before the reflected wave reaches a distance of about one penetration depth under the surface.[11] The resulting acoustic wave thus possesses a bipolar profile: a compressive maximum followed by a tensile component.[11] This is clearly visible in Fig. 10, which shows the evolution of the pressure inside the target for a fluence below the threshold for ablation.

However, it is also apparent that the tensile component is weaker and less sharp than the compressive one. For the excellent stress confinement achieved here ($\alpha c\Delta t\simeq 0.08$), a symmetric profile would be expected. This indicates that, even at modest fluences, the pressure waves are too intense to be reflected elastically from the free surface: a fraction of the energy of the incident wave is used for the creation of defects or inelastic deformations in the surface region during reflection.

Figure 11 shows that, at higher fluences (above the threshold for ablation), the pressure profile becomes unipolar: the

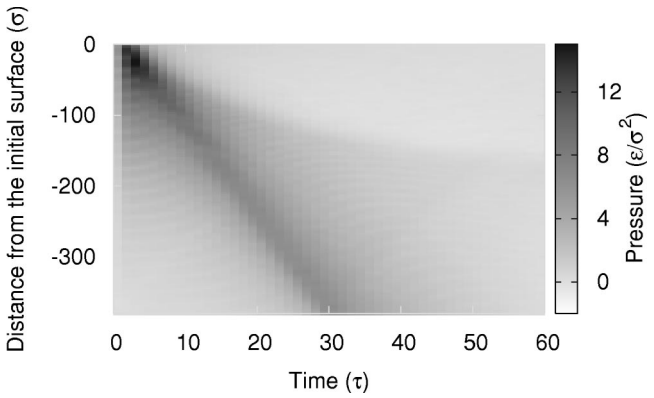

FIG. 11. Pressure in the target as a function of time and position; $F=450\epsilon/\sigma$, $\alpha=0.01\sigma^{-1}$.

tensile component disappears completely. The wave incident on the free surface is thus totally dissipated in the surface region so that no reflection occurs. The tensile stress region visible in this figure is not induced by an elastic wave, but by the progression of the melt front which initially propagates at the speed of sound, and later on slows down and finally stops around $y=-120\sigma$.

Figure 12 establishes the preceding observations on a more quantitative basis by showing the dependence on fluence of the peak maximum and minimum pressures ($P_{\max}$ and $P_{\min}$, respectively) measured inside the sample. $P_{\max}$ is found to grow linearly with fluence, as expected for a thermoelastic wave generation process. In the case of an instantaneous heating, $P_{\max}=\alpha\Gamma F$ with Γ the Grüneisen parameter of the material. However, the behavior of $P_{\min}$ is much more complex: it initially decreases until $F=90\epsilon/\sigma$, then grows and finally saturates around $P_{\min}=-0.45\epsilon/\sigma^2$ for $F>200\epsilon/\sigma$. As stated earlier, if reflection on the free surface is total, $P_{\min}$ should also decrease linearly with fluence for such short pulses. The increase in $P_{\min}$ thus indicates again that the reflection of the pressure wave is not elastic above a certain threshold. Indeed, in the interval $90\epsilon/\sigma<F<150\epsilon/\sigma$, we observe a damage-without-ablation regime — small pores nucleate near the surface, but in insufficient number to cause ablation — while for $F<90\epsilon/\sigma$, the sample remains intact after the reflection of the wave. This thus establishes that the increase of $P_{\min}$ at high fluence is caused by the formation of defects in the surface area of the target. The behavior of $P_{\min}$ is very similar to that observed in simulations of ablation in organic solids (Ref. 19), except that the peak in the tensile pressure does not coincide with the ablation threshold in our simulations but, rather, corresponds to a damage threshold.

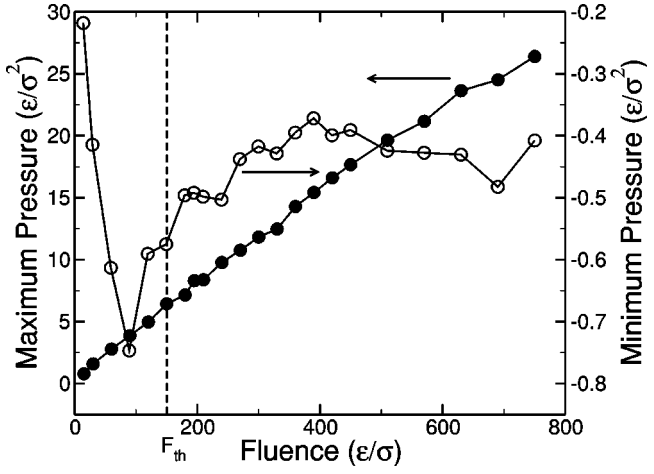

FIG. 12. Maximum (filled circles) and minimum (empty circles) pressure reached inside the target $\alpha=0.01\sigma^{-1}$. The dashed line marks the threshold for ablation.

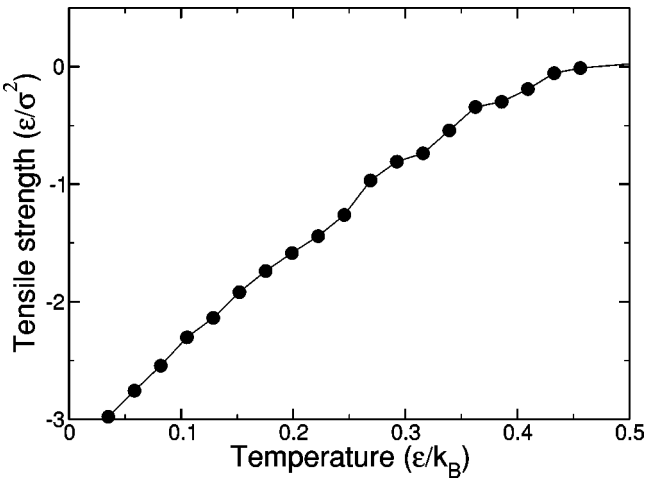

FIG. 13. Tensile strength of the 2D Lennard-Jones solid as a function of temperature.

The fluence at which the tensile wave disappears can be calculated by considering the dependence on temperature of the elastic properties of the material. Indeed, because the tensile component of the pressure wave results from the reflection of the compressive wave on the free surface, $P_{\min}$ cannot assume values lower than the tensile strength of the material in the surface region. Following Ref. 33, we consider that the tensile (spall) strength at a given temperature is the minimum pressure reached on the corresponding isotherm. Further stretching of the material along this isotherm would push the material in a region of negative compressibility, where the system is unstable against density fluctuations, hence inducing its failure.

The results, presented in Fig. 13, show that the tensile strength is an increasing function of temperature that goes to zero as temperature reaches $0.45\epsilon/k_B$. Thus, if the surface region is hotter than this value during the emission of the compressive waves, the reflection will be completely inelastic and all the energy of the incident wave will be dissipated through the creation of defects. If we require the tensile strength to vanish at a depth of α^{-1} under the surface to ensure a complete dissipation of the incident compressive wave (remembering that the tensile wave is fully formed only at α^{-1} under the surface), we find that no tensile wave should form for fluences higher than $F=210\epsilon/\sigma$ at $\alpha=0.01\sigma^{-1}$. We see from Fig. 12 that this fluence corresponds to the beginning of the saturation regime of $P_{\min}$. For fluences higher than this value, the tensile pressure inside the sample is not caused by the passage of an acoustic wave, but

results from the expansion speed difference between the solid, nonablated target, and the expanding liquid material which induces tension at the interface between the two phases.

We have demonstrated that the formation of tensile pressure waves does not occur at high fluence because of the thermal softening of the material. This possibility was proposed by Zhigilei and Garrison[19] based on simulations of ablation of organic solids. Thus, tensile-wave-mediated effects play a role in ablation only for fluences around the ablation threshold. The dissipation of the energy contained in the compressive wave incident on the surface will certainly have an impact on the expansion dynamics and on the ejection of material at higher fluences. However, in our simulations, the energy contained in this wave is at most 20% of the total injected energy. The influence of this contribution on the dynamics of the surface regions is thus expected to be modest.

B. Mechanisms of ablation

It was shown in the preceding sections that different regions form in the target during the ablation process. These regions differ in their expansion dynamics and morphology, and in the thermodynamical relaxation path they follow. This suggests that different ablation mechanisms may be effective in each of these regions. We now demonstrate that it is indeed the case. The thermodynamical trajectories of the different regions of the target indicate that four different ablation mechanisms are present: spallation, homogeneous nucleation, fragmentation, and vaporization. They are discussed below in order of increasing energy.

1. Spallation

Spallation is the result of internal failure due to the creation of defects induced by tensile stresses. This phenomenon is routinely observed in ablation experiments on gels[18] and biological tissues.[3] Simulations of ablation of organic solids in the stress-confinement regime have been interpreted in terms of a spallationlike process.[19] In the case of more cohesive solids (metals, semiconductors), Schäfer *et al.*[32] recently proposed that front-side spallation could also be important.

While spallation is sometimes used to describe failure in solids as well as in liquids, we restrict the use of the term to describe the fracture of a solid in which the tensile strength is exceeded. In contrast, the failure of a liquid under tension by nucleation of gas bubbles (while the system is in a metastable state) will be referred to as cavitation, or simply homogeneous nucleation.

In Sec. III A 3 it was shown that important tensile waves form at fluences close to the threshold for ablation. Spallation should thus be observable in this regime. Indeed, as shown in Fig. 14, ablation proceeds by the ejection of complete layers of material at the threshold fluence.

This behavior is very similar to that observed in simulations of ablation of organic solids,[19] in laser-induced backspallation experiments,[34] and in computer simulations of flyer-plate collisions.[35] In all cases, the passage of a tensile wave induces fractures parallel to the surface of the sample and ejection of complete layers of material. The first snapshot in Fig. 14 shows the state of the system at $t=50\tau$. By then, the tensile wave has already crossed most of the sample and a large number of small pores are visible near the surface. During the next 100τ's they grow and coalesce to finally cause the ejection of the complete surface layer. No voids form very close to the surface because the tensile wave only develops as it travels towards the bulk.[11] The ejected layer eventually breaks up as the expansion continues. Figure 15 confirms in a quantitative manner that spallation is responsible for ablation in this regime.

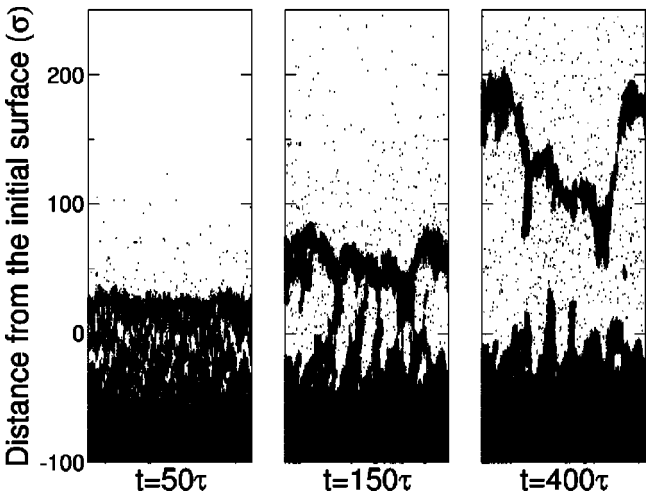

FIG. 14. Snapshot of the system showing ablation by a spallation mechanism; $F=150\ \epsilon/\sigma$, $\alpha=0.01\sigma^{-1}$.

The trajectories in the ρ-T plane show that absorption of the laser pulse initially heats the slice up to a very high temperature (larger than the critical temperature). However, expansion quickly sets in and lowers the temperature below

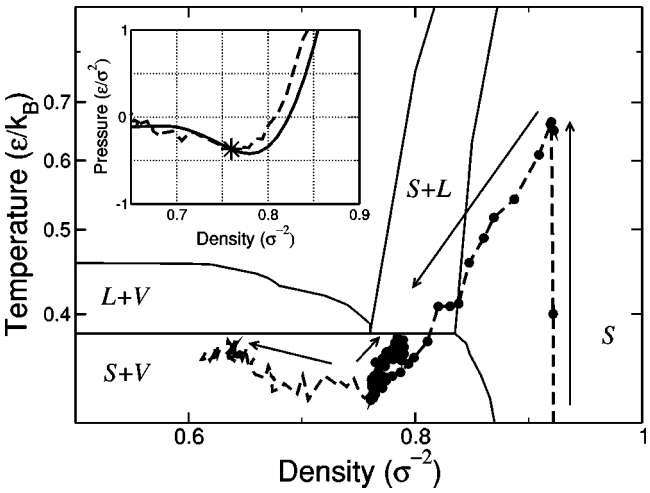

FIG. 15. Typical thermodynamical evolution for regions of the target where spallation occurs, for $F=150\ \epsilon/\sigma$, $\alpha=0.01\sigma^{-1}$, $E_{\mathrm{eff}}=0.95\epsilon/\sigma^2$. Dashed line: average branch; filled circles: condensed branch. Arrows indicate the flow of time. Inset: average trajectory in the ρ-P plane (dashed line) and $T=0.36$ isotherm (solid line). The star indicates the point of fracture.

the triple point after a small incursion into the solid-liquid coexistence region. The inset shows that the tensile wave reaches this slice when $\rho \simeq 0.81\sigma^{-2}$, then induces further stretching of the material. The split between the average and condensed branches in the ρ-T plane indicates that the material finally fractures around $\rho \simeq 0.76\sigma^{-2}$. After the failure, the temperature rises significantly and the density on the condensed branch increases, indicating that the stretching induced by the passage of the tensile wave causes some of the thermal energy of the slice to be momentarily converted into elastic energy. During the fracture process, part of the stored elastic energy is converted back into heat, causing the observed rise of both temperature and density on the condensed branch. Nevertheless, a decrease of the average density is observed because of the opening of voids. The coalescence of these will later induce ablation.

Following the definition of the tensile strength given in Sec. III A 3, failure of the material should occur when the system reaches the minimum pressure of the isotherm on which it lies at this moment. The inset of Fig. 15 confirms that this is indeed the case by showing in the ρ-P plane, the average trajectory of the slice together with the $T = 0.36\epsilon/k_B$ isotherm (on which spallation occurs). The failure point is indeed very close to the pressure minimum of this isotherm; fracture and subsequent ablation are thus caused by the loss of mechanical stability of the expanding system, i.e., again spallation. The pores grow until the stress inside this region is completely relieved.

Spallation in the solid phase was only observed in a small range of fluences around the threshold fluence. Further, ''good'' stress confinement is required for strong pressure waves to develop; hence this mechanism is probably restricted to pico and femtosecond pulses. We saw that, as fluence increases, the amplitude of the tensile wave propagating inside the sample decreases and eventually vanishes. As this occurs, the contribution of spallation to the total yield diminishes to the profit of homogeneous nucleation, which we discuss next.

2. Homogeneous nucleation

As seen in Sec. III A 2, when higher densities of energy are injected into the system, the relaxation does not proceed within the solid region anymore but, rather, above the triple point: the material melts and later crosses the binodal line, entering the liquid-vapor metastable region of the phase diagram. In this region, the pressure inside the liquid is lower than the saturation vapor pressure. When this occurs, the homogeneous liquid state is no longer the most stable configuration because the free energy of the gas phase becomes lower than that of the liquid.[36] However, the liquid state is still a local free-energy minimum, so an energy barrier has to be crossed for gas domains to nucleate (except at the spinodal line where the barrier vanishes). For long enough waiting times, gas bubbles will thus form inside the liquid through a process called homogeneous nucleation.

The decrease of the pressure below the saturated vapor value can be induced by the passage of a tensile wave or simply by adiabatic relaxation during the expansion. If high nucleation rates are reached, ablation can be induced by the

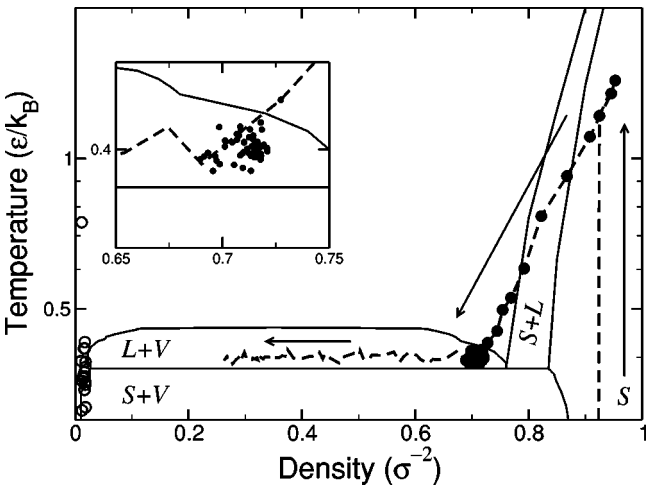

FIG. 16. Typical thermodynamical evolution for regions of the target where homogeneous nucleation occurs $E_{\text{eff}} = 1.7\epsilon/\sigma^2$. Dashed line: average branch; filled circles: condensed branch; empty circles: gas branch. Inset: zoom on the trajectory at the entrance of the metastable region.

rapid transition from a superheated liquid state to a mixture of vapor and liquid droplets through a process referred to as phase explosion or homogeneous boiling. Since Kelly and Miotello[14–16] showed that phase explosion is the only thermal mechanism that occurs on a sufficiently small timescale to explain the ejection of liquid droplets in short-pulse experiments, phase explosion is widely considered as the most common cause of ablation in the nano to femtosecond regimes.[5,14–16,37–39] Phase explosion has also been inferred from the properties of the plume in computer simulations of ablation of organic liquids,[19] but was directly observed only recently in molecular-dynamics simulations by following the thermodynamical evolution of the system.[21] By analogy with liquids, ablation could also possibly occur by hydrodynamic sputtering resulting from the collapse of gas bubbles that did not reach the critical size;[4,18] this mechanism has, however, not been observed in the present simulations. We now show that the growth of gas-filled bubbles in region II of Figs. 3 and 4 is caused by a homogeneous nucleation process and that ablation follows by homogeneous boiling.

Figure 16 shows the thermodynamical signature of a phase explosion process leading to ablation. Once again, the slice is heated at constant volume up to a very high, supercritical temperature. The rarefaction wave then reaches the slice and a quasiadiabatic relaxation process begins. It proceeds through the solid-liquid coexistence region before the material completely melts upon entering the one-phase liquid region. It can be seen that the system then enters the liquid-vapor metastable region, where the liquid is under tension. Note that no voids are present in the slice before entering the metastable region: the average and condensed branches are completely superimposed. However, the separation of the average and condensed branches, combined with the appearance of the gas branch, confirm that gas-filled bubbles begin to nucleate inside the slice right after the binodal is crossed. A phase separation process then sets in: the condensed phase gradually converts into gas by nucleation and growth of gas

regions. However, the timescale for this transformation to take place is very long, so liquid droplets can persist in the plume for a very long time. Because the free-energy barrier for the nucleation of gas bubbles is very low for any significant incursion into the metastable region (and finally vanishes at the spinodal line),[40] nucleation proceeds at a large rate. The growth and coalescence of these gas-filled bubbles, clearly visible in region II of Figs. 3 and 4, will eventually cause the ablation of large liquid droplets.

Despite wide acceptance of this mechanism, there is still some confusion in the literature about the conditions in which phase explosion occurs. While it is recognized that a rigorous criterion should be based on the approach of the spinodal line, it is often assumed that a sufficient condition for important density fluctuations and homogeneous nucleation to take place is that the peak temperature inside the target exceeds $T=0.9T_c$.[14–16,37–39] This criterion is correct for slow heating rates at nearly constant pressure; however, it does *not* apply in stress-confinement conditions typical of short-pulse laser ablation experiments because heating is isochoric so that the system is actually pushed *away* from the metastable region in the first place. In this case, the occurence of homogeneous nucleation depends, rather, on the relaxation path followed during the relaxation phase. Indeed, the system can be heated to temperatures higher than T_c but still relax within the solid regions of the phase diagram without ever entering the metastable region (the only region in which homogeneous nucleation is possible). An example of this behavior is given in Fig. 15. In fact, the important quantity for the occurrence of phase explosion is the nucleation rate[41]

$$J = A \exp\left(-\frac{\Delta G}{k_B T} \right), \tag{5}$$

where A is a kinetic factor that depends weakly on temperature and ΔG is the free-energy barrier for nucleation.[41] As this free-energy barrier vanishes for all points along the spinodal line, a temperature close to the critical temperature is not required for significant nucleation to occur; the only condition is to reach deep enough into the metastable region.

In conditions of isochoric heating and adiabatic expansion, phase explosion can occur for relaxation along isentropes intersecting the binodal line between the triple and critical points. Knowledge of the equation of state of the material is then sufficient to compute both these limits and to obtain the energy density interval for which homogeneous nucleation takes place. However, in typical laser ablation experiments, the expansion is nonadiabatic because the emission of pressure waves during the relaxation induces faster-than-adiabatic cooling. The adiabatic hypothesis thus underestimates the energy required for phase explosion to occur.

For good enough thermal confinement, phase explosion can also occur with longer pulses. However, in this case, the material follows a different thermodynamical path than that presented in Fig. 16: expansion occurs during heating as the pulse length is increased until the expansion eventually proceeds along the binodal line for long enough pulses.

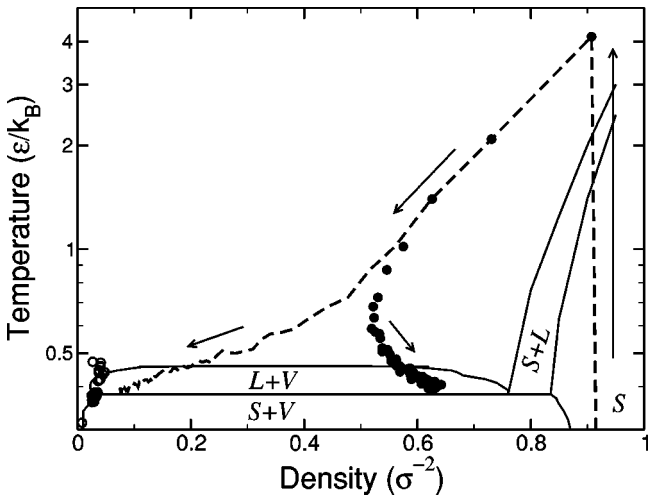

FIG. 17. Typical thermodynamical evolution for regions of the target where fragmentation occurs $E_{\text{eff}}=5.4\epsilon/\sigma^2$. See Fig. 16 for the definition of symbols and lines.

As discussed briefly in Ref. 21, our simulations confirm that phase explosion by homogeneous nucleation of bubbles is indeed effective in short-pulse laser irradiation conditions at moderate energies. We will now see that, at higher energies, fragmentation replaces phase explosion as the dominant ablation mechanism.

3. Fragmentation

In a preliminary report of this work,[21] we have shown that fragmentation of a super-critical fluid could account for a significant part of the total ablation yield in short-pulse conditions. We now proceed with a detailed analysis of this mechanism.

Fragmentation is the process whereby an initially homogeneous medium decomposes into a collection of clusters as a result of impact or expansion. This mechanism has been observed in a wide range of systems under large strain rates: continuous systems under adiabatic expansion,[42–45] isochoric heating of small droplets,[46–48] free-jet expansion of liquids,[49,50] etc. In laser ablation conditions, photomechanical fragmentation occurs as a result of the conversion of the stress induced by the constant volume heating into strain during the subsequent expansion.[21]

We first demonstrate that ablation in the high-expansion-speed regime (region III) is not induced by a photothermal process; we will then show that fragmentation is responsible for ablation in this case. Figure 17 shows the thermodynamical evolution of a slice in this regime. The heating rate is now so intense that the material is pushed into a strongly superheated solid state. Melting occurs at the very beginning of the relaxation and the material then expands in a supercritical fluid state. Soon after, voids begin to appear. The split between the average and condensed branches — indicating the onset of pore creation — now occurs way *above* the binodal line, implying that the system has already decomposed by the time the metastable region is reached. This therefore *excludes* homogeneous nucleation as the mecha-

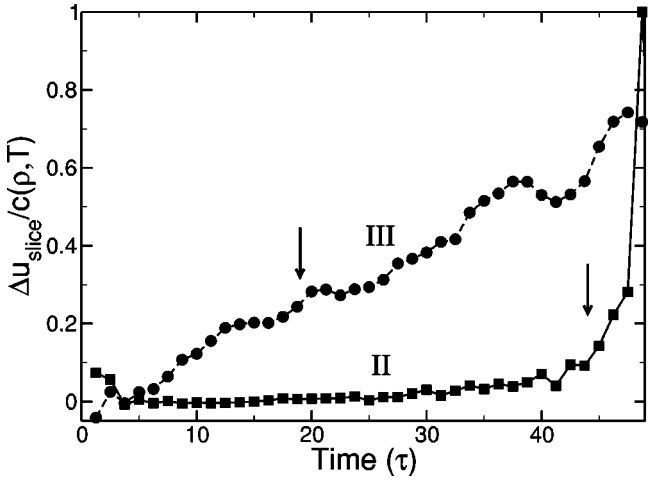

FIG. 18. Ratio of the differential expansion speed within a single slice to the instantaneous speed of sound with $\alpha = 0.01\sigma^{-1}$. Squares: $E_{\text{eff}} = 1.05\epsilon/\sigma^2$ (region II); circles: $E_{\text{eff}} = 3.6\epsilon/\sigma^2$ (region III). Arrows indicate the onset of void formation.

nism responsible for ablation in this regime. Further, region III of Fig. 4 shows that large clusters are present in the plume, so vaporization must also be excluded. Since Miotello and Kelly[16] showed that homogeneous nucleation is the only photothermal process relevant to the description of ablation in short-pulse conditions, we must therefore conclude that ablation is not caused by a photothermal mechanism in this regime.

We saw in Sec. III A 2 that, in region III, the expansion speed is a strongly dependent function of the injected energy, and hence of the position inside the target. In this case, the exponential heating profile induces very important strain rates ($\eta = du/dy$) and thus creates ideal conditions for the occurrence of fragmentation.

This is shown in Fig. 18, where we plot the time dependence of the differential expansion speed between the two ends of a single slice relative to the instantaneous speed of sound. We see that, for expansion in region III (circles), the ratio increases quickly and reaches about a third by the time voids begin to form. As mass transport necessarily occurs at a speed lower than the speed of sound, diffusion will not be efficient enough to balance out anything but the smallest density fluctuations. In this case, the equilibrium structure of the fluid will be lost as new surfaces appear inside the liquid. In contrast, in region II (squares), where the expansion speed depends only weakly on the injected energy (see Fig. 5), the ratio remains very low until the system enters the liquid-vapor metastable region. At this moment, the speed of sound drops abruptly so that the ratio suddenly increases. In this case, the expansion can be considered quasi-static and diffusion preserves the equilibrium structure of the fluid up to the entrance of the metastable region.

Thus, ablation is *not* caused by a photothermal process in region III; we have also shown that the conditions required for fragmentation are present. We now demonstrate explicitly, through an analysis of the fragment mass distribution of the plume, that fragmentation is indeed responsible for ablation.

A simple model for the fragmentation of continuous systems has been proposed by Ashurst and Holian.[44] In this model, the elastic potential energy ϕ_{elast} stored in the system as a result of expansion is converted into surface energy ϕ_{surf} by a bond-breaking mechanism. In the context of a two-dimensional uniaxial expansion, we have, for a fragment of side L:

$$\phi_{\text{elast}} = \frac{1}{2} B_0 L_0^2 (\eta t)^2, \tag{6}$$

where $B_0 = \rho_0 c_0^2$ is the bulk modulus and

$$\phi_{\text{surf}} = 4\rho L r_0 \gamma, \tag{7}$$

with r the bond length and γ the surface energy density. The subscript 0 indicates quantities evaluated at the beginning of the expansion, while others are evaluated at fragmentation time.

Fragmentation occurs when the elastic energy stored in a region of the target is equal to the surface energy it would have if isolated. At this point, the excess elastic energy is converted into surface energy and fragments are created. Within this model, it can be shown that the mean cluster mass is given by[44]

$$M = 4\zeta\rho (r_0 \gamma)^{2/3} \eta^{-4/3}, \tag{8}$$

where the geometric factor $\zeta \sim 1$ allows for arbitrary cluster shapes. Equation (8) expresses the fact that higher strain rates cause more elastic energy to be stored inside the material and hence more energy to be dissipated by the opening of voids. However, Eq. (8) also says that fragmentation does not depend only on the elastic energy stored in the sample (itself a function of the strain): it also depends explicitly on the speed gradient (strain rate) imposed to the system. Fragmentation is thus a nonequilibrium process and does not occur in the quasistatic expansion limit. It should be noted that since the equilibrium structure of a supercritical fluid is not homogeneous at moderate densities, decomposition of the fluid into fragments could still occur even at low strain rate, a process called ''trivial fragmentation.''[45]

The same scaling law between the size of clusters and the strain rate (but with a different prefactor) can actually be obtained using the Grady model.[44,46,51] In this model, the sum of expansion and surface energies is minimized; for high enough strain rates, the most stable configuration is the fragmented one, i.e., it becomes more energetically favorable for the system to fragment than to continue expanding homogeneously. This scaling law thus constitutes a strong signature of fragmentation.

We therefore computed the mean mass of clusters as a function of strain rate at their formation depth in the high expansion speed region for two different fluences. This data is shown in Fig. 19 together with the prediction of Eq. (8),

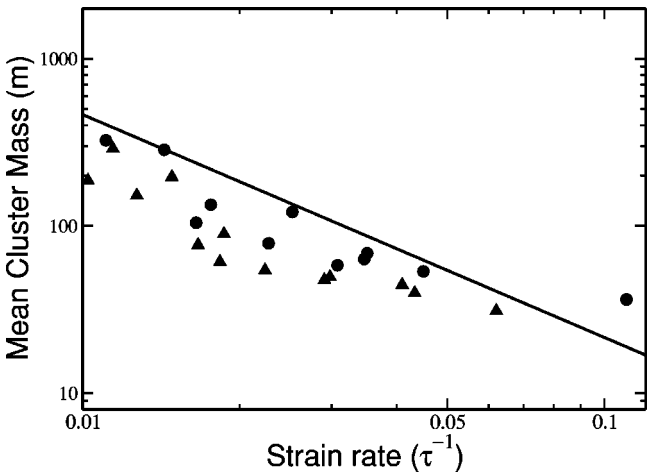

FIG. 19. Mean cluster mass versus local strain rate for $\alpha = 0.01\sigma^{-1}$. Circles: $F = 750\epsilon/\sigma$; triangles: $F = 900\epsilon/\sigma$. The solid line is Eq. (8).

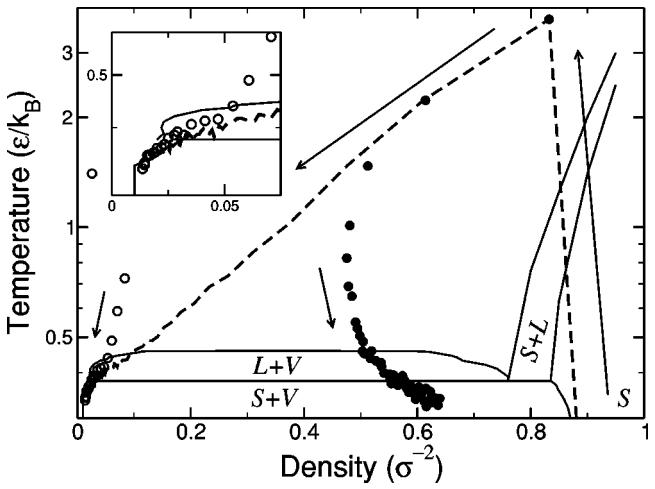

FIG. 20. Typical thermodynamical evolution for regions of the target where vaporization occurs $E_{\text{eff}} = 7.7\epsilon/\sigma^2$. Inset: enlargement of the low-T-low-ρ region. See Fig. 16 for the definition of symbols and lines.

where we have used $\zeta = \pi/4$ (circular clusters) and $\rho = 0.6\sigma^{-1}$. The surface energy density γ is taken to be the mean energy of a bond at breakup time multiplied by the number of broken bonds per atom. The data clearly reproduce the predicted power law behavior. Further, the prefactor obtained from a fit to the data agrees to within 30% with the one deduced from Eq. (8). Given the simple nature of the model, the fit is certainly excellent and clearly indicates that ablation is determined by the expansion rate of the material and is thus caused by fragmentation.

It was shown in Sec. III A 2 that strongly energy dependent expansion speeds are measured for supercritical relaxations paths. The large strain rates present in the region of the target relaxing along such paths (region III) thus produce ideal conditions for the occurrence of fragmentation. Indeed, all fragmenting trajectories were observed in this regime. A rough estimate of the minimum energy density for which fragmentation occurs is thus given by the energy required for the material to reach the critical point isentrope. However, by contrast with thermal mechanisms, fragmentation does not depend only on the relaxation isentrope, but also on the strain rates induced in the target. As the flow speed is mainly determined by the effective energy, high strain rates will result from large absorption coefficients. In this case, the balance between fragmentation and homogeneous nucleation will tilt in favor of the former: some slices relaxing on isentropes crossing the binodal between the triple and critical points will fragment before entering the metastable zone. However, at small absorption coefficient, phase explosion will prevail up to the critical point isentrope and fragmentation will be limited to supercritical conditions.

4. Vaporization

At high enough energies, the surface layer of the target is completely atomized and expands at very high speed (see part IV of Fig. 5). Very few clusters are present in this part of the plume. The evolution of a slice in this regime is presented in Fig. 20.

We see from this figure that the condensed and average branches split at a very early time and that the average and gas branches merge soon after, indicating that the slice as a whole is behaving as a gas. As stated earlier, expansion occurs along perfect-gas-like isentropes in this regime. The trajectory thus simply illustrates a vaporization process. Here, vaporization is not used in the sense of the Hertz-Knudsen equation, which describes evaporation or sublimation from the outer surface of a material, but to describe the complete dissociation of the topmost layers of the target when the injected energy is close to (or exceeds) the cohesive energy of the material. Note that only about 5% of the atoms from the slice are contained in clusters at the end of the simulation so the behavior of the condensed branch is not very meaningful.

C. Ablation depth

Armed with the knowledge of the ablation mechanisms identified in the previous section, it is possible to predict, for high enough fluences, the dependence of the ablation depth on fluence, a very important quantity for practical applications.

We showed earlier that the mechanical and thermodynamical evolution of a slice is, in a first approximation, only a function of the effective energy (see Sec. III A 2 for the definition of E_{eff}). Away from the threshold fluence, phase explosion is the ablation mechanism requiring the smallest amount of energy. The ablation and phase explosion thresholds should thus be the same: slices which possess effective energies greater than the threshold ($E_{\text{eff-th}}$) should experience ablation by phase explosion, fragmentation or vaporization, while slices which possess effective energies less than the threshold will relax to a solid state without being ejected. Following the discussion of Sec. III B 2, $E_{\text{eff-th}}$ should be given by the energy density required to reach the triple point isentrope from the initial state.

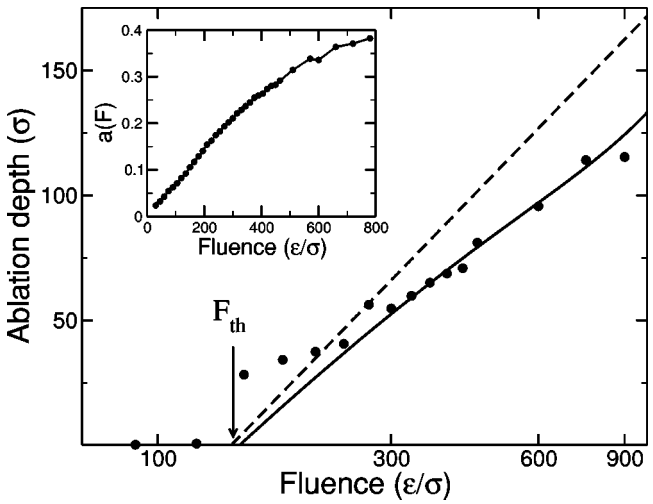

FIG. 21. Ablation depth $\alpha=0.01\sigma^{-1}$. Dashed line: Eq. (11), continuous line: Eq. (10) with $E_{\text{eff}}=1.16\epsilon/\sigma^2$. Inset: Efficiency of the acoustic conversion for $\alpha=0.01\sigma^{-1}$.

Since the effective energy density at depth y is approximately given by

$$E_{\text{eff}}(y)=[1-a(F)]\alpha F e^{-\alpha y}, \tag{9}$$

where $a(F)$ is the efficiency of the acoustic conversion at this fluence $[a(F)=E_{\text{waves}}(F)/E_{\text{laser}}(F)]$, the depth at which the effective energy is equal to the threshold for ablation is

$$y(F)=\alpha^{-1}\ln\left(\frac{\alpha F[1-a(F)]}{E_{\text{eff-th}}}\right). \tag{10}$$

The quantity $a(F)$ was calculated independently as follows. We constructed a sample composed of the usual target on which a very thick layer of the same material was placed. However, this new layer was not allowed to absorb the incoming laser pulse (i.e., is transparent). Pressure-absorbing boundary conditions were applied to both ends of the target, while periodic boundary conditions were used in the x direction. Because the two regions have the same acoustic impedance, the component of the pressure wave that is usually reflected from the free surface of the absorbing medium is now transmitted into the transparent material; the other component still proceeds toward the bottom of the sample. The acoustic energy (E_{waves}) is obtained by measuring the drop in the total energy of the system after the absorption of the pressure waves by the special boundary conditions, which is then be divided by E_{laser} to yield a. (One cannot compute E_{waves} with the usual sample, because the reflection of the wave on the free surface is not elastic at high fluences. The acoustic energy collected at the bottom of the sample would thus be less than the acoustic energy initially emitted.) The result is shown in the inset to Fig. 21.

For comparison, if we neglect the effect of energy loss by the generation of pressure waves, we obtain the well known expression

$$y(F)=\alpha^{-1}\ln\left(\frac{\alpha F}{(\alpha F)_{\text{th}}}\right). \tag{11}$$

In Fig. 21 we show a comparison of the data from our simulations with both expressions. An excellent fit is obtained using Eq. (10) with $E_{\text{eff-th}}=1.16\epsilon/\sigma^2$. This value corresponds to the onset of the phase explosion region (see region II of Fig. 5 and Sec. III B 2). In contrast, Eq. (11) overestimates the energy available for ablation and hence the total yield. The cooling induced by the pressure wave formation is thus important enough to notably affect the ejection of atoms from the target.

Note that both expressions underestimate the ablation depth for fluences around the threshold. This discrepancy is due to contributions from spallation effects. Indeed, at the threshold fluence, homogeneous nucleation only occurs within a few slices near the surface but many are ejected following spallation. This proportion gradually increases in favor of homogeneous boiling as the fluence increases. However, it is very difficult to predict the spallation depth because the dynamics of the pressure wave formation in a material with strongly position (temperature) dependent properties is very difficult to estimate. Nevertheless, as the fluence increases, the tensile waves disappear, so phase explosion becomes totally responsible for the onset of ablation and Eq. (10) becomes correct. It should be noted that recondensation of part of the ejected material on the target — which could somewhat decrease the ablation depths observed here — is not taken into account because it occurs on a timescale much beyond our simulations.

IV. SUMMARY

The ablation of solids under femtosecond laser pulses has been studied using molecular-dynamics simulations. Our calculations show that the reaction of the target is strongly dependent on the energy density injected by the laser through the thermodynamical trajectory by which the matter relaxes. This causes the formation of distinct regions with specific expansion dynamics at different depths under the surface of the target. Temperature variations of the mechanical properties of the target are also shown to cause changes in the shape of the generated pressure waves; from bipolar at low fluence to unipolar at high fluence. This implies that tensile-wave-mediated effects are only effective at low fluences. Indeed, spallation is only observed when the tensile component of the pressure wave is sufficiently important. Phase explosion is the main mechanism responsible for ablation at moderates fluences. This mechanism occurs in slowly expanding regions of the target and is able to produce conditions in which Newton rings are expected to form. For high strain rates, the plume is formed by mechanical fragmentation of the expanding medium. Complete vaporization of the surface layers is also observed. These mechanisms typically occur simultaneously at different positions under the surface of the target. Finally, a formula for the ablation depth is presented and it is shown that the pressure waves formation must be considered in order to predict the ablation yield correctly.

ACKNOWLEDGMENTS

We thank Patrick Lorazo, Ralf Meyer, and Michel Meunier for numerous enlightening discussions. This work has been supported by grants from the Canadian Natural Sciences and Engineering Research Council (NSERC) and Québec's *Fonds Québécois de la Recherche sur la Nature et les Technologies* (FQRNT). We are indebted to the *Réseau Québécois de Calcul de Haute Performance* (RQCHP) for generous allocations of computer resources.

*Electronic address: danny.perez@umontreal.ca
†Electronic address: Laurent.Lewis@UMontreal.CA

[1] K. Furusawa, K. Takahashi, H. Kumagai, K. Midorikawa, and M. Obara, Appl. Phys. A: Mater. Sci. Process. **69**, S359 (1999).
[2] F. Korte, S. Nolte, B. Chichkov, T. Bauer, G. Kamlage, T. Wagner, C. Fallnich, and H. Welling, Appl. Phys. A: Mater. Sci. Process. **69**, S7 (1999).
[3] I. Itzkan, D. Albagli, M. Dark, L. Perelman, C. von Rosenberg, and M. Fields, Proc. Natl. Acad. Sci. U.S.A. **92**, 1960 (1995).
[4] A. Oraevsky, S. Jacques, and F. Tittel, J. Appl. Phys. **78**, 1281 (1995).
[5] K. Sokolowski-Tinten, J. Bialkowski, A. Cavalleri, D. von der Linde, A. Oparin, J. M. ter Vehn, and S. Anisimov, Phys. Rev. Lett. **81**, 224 (1998).
[6] B. Rethfeld, K. Sokolowski-Tinten, and D. von der Linde, Phys. Rev. B **65**, 092103 (2002).
[7] A. Kaiser, B. Rethfeld, M. Vicanek, and G. Simon, Phys. Rev. B **61**, 11 437 (2000).
[8] J. Graves and R. Allen, Phys. Rev. B **58**, 13 627 (1998).
[9] K. Sokolowski-Tinten, J. Bialkowski, M. Boing, A. Cavalleri, and D. von der Linde, Phys. Rev. B **58**, 11 805 (1998).
[10] J. Callan, A.-T. Kim, C. Roeser, and E. Mazur, Phys. Rev. B **64**, 073201 (2001).
[11] J. C. Bushnell and D. J. McCloskey, J. Appl. Phys. **39**, 5541 (1968).
[12] J. I. Etcheverry and M. Mesaros, Phys. Rev. B **60**, 9430 (1999).
[13] V. Zhakhovskii, K. Nishiara, S. Anisimov, and N. Inogamov, JETP Lett. **71**, 167 (2000).
[14] R. Kelly and A. Miotello, Appl. Surf. Sci. **96-98**, 205 (1996).
[15] A. Miotello and R. Kelly, Appl. Phys. Lett. **67**, 3535 (1995).
[16] A. Miotello and R. Kelly, Appl. Phys. A: Mater. Sci. Process. **69**, 569 (1999).
[17] B. N. Chichkov, C. Momma, S. Nolte, F. von Alvensleben, and A. Tünnermann, Appl. Phys. A: Mater. Sci. Process. **63**, 109 (1996).
[18] G. Paltaud and H. Schmidt-Kloiber, Appl. Phys. A: Mater. Sci. Process. **62**, 303 (1996).
[19] L. V. Zhigilei and B. J. Garrison, J. Appl. Phys. **88**, 1281 (2000).
[20] F. Vidal, T. Johnston, S. Laville, O. Barthélemy, M. Chaker, B. L. Drogoff, J. Margot, and M. Sabsabi, Phys. Rev. Lett. **86**, 2573 (2001).
[21] D. Perez and L. J. Lewis, Phys. Rev. Lett. **89**, 255504 (2002).
[22] M. Allen and D. Tildesley, *Computer Simulation of Liquids* (Oxford Science Publications, Oxford, 1987).
[23] L. V. Zhigilei and B. J. Garrison, in *Multiscale Modeling of Materials*, edited by T. Diaz de la Rubia *et al.*, Mater. Res. Soc. Symp. Proc. No. 538 (Materials Research Society, Warrendale, 1999), p. 491.
[24] D. von der Linde, K. Sokolowski-Tinten, and J. Bialkowski, Appl. Surf. Sci. **109**, 1 (1997).
[25] J. Hoshen and R. Kopelman, Phys. Rev. B **14**, 3438 (1976).
[26] B. Smit and D. Frenkel, J. Chem. Phys. **94**, 5663 (1991).
[27] A. Z. Panagiotopoulos, Mol. Phys. **61**, 813 (1998).
[28] H. Schäfer, A. E. Mark, and W. F. van Gunsteren, J. Chem. Phys. **113**, 7809 (2002).
[29] L. Landau and E. Lifshits, *Course of Theoretical Physics VI: Fluid Mechanics* (Pergamon Press, Oxford, 1982).
[30] S. Anisimov, N. Inogamov, A. Oparin, B. Rethfeld, M. Ogawa, and V. Fortov, Appl. Phys. A **69**, 617 (1999).
[31] A. Cavalleri, K. Sokolowski-Tinten, J. Bialkowski, M. Schreiner, and D. von der Linde, J. Appl. Phys. **85**, 3301 (1999).
[32] C. Schäfer, H. M. Urbassek, and L. V. Zhigilei, Phys. Rev. B **66**, 115404 (2002).
[33] E. Dekel, S. Eliezer, Z. Henis, E. Moshe, A. Ludmirsky, and I. Goldberg, J. Appl. Phys. **84**, 4851 (1998).
[34] H. Tamura, T. Kohama, K. Kondo, and M. Yoshida, J. Appl. Phys. **89**, 3520 (2001).
[35] N. Wagner, B. Holian, and A. Voter, Phys. Rev. A **45**, 8457 (1992).
[36] V. P. Carey, *Liquid-vapor Phase-change Phenomena* (Hemisphere, Washington, D.C., 1992).
[37] J. Yoo, S. Jeong, X. Mao, R. Grief, and R. Russo, Appl. Phys. Lett. **76**, 783 (1999).
[38] J. Yoo, S. Jeong, R. Grief, and R. Russo, J. Appl. Phys. **88**, 1638 (2000).
[39] N. Bulgakova and A. Bulgakov, Appl. Phys. A: Mater. Sci. Process. **73**, 199 (2000).
[40] V. K. Shen and P. G. Debenedetti, J. Chem. Phys. **114**, 4149 (2001).
[41] V. Shen and P. Debenedetti, J. Chem. Phys. **111**, 3581 (1999).
[42] B. Holian and D. E. Grady, Phys. Rev. Lett. **60**, 1355 (1988).
[43] C. O. Dorso and A. Strachan, Phys. Rev. B **54**, 236 (1996).
[44] W. T. Ashurst and B. L. Holian, Phys. Rev. E **59**, 6742 (1999).
[45] S. Toxvaerd, Phys. Rev. E **59**, 6742 (1999).
[46] J. A. Blink and W. G. Hoover, Phys. Rev. A **32**, 1027 (1985).
[47] A. Vicentini, G. Jacucci, and V. Pandharipande, Phys. Rev. C **31**, 1783 (1985).
[48] A. Strachan and C. O. Dorso, Phys. Rev. C **58**, R632 (1998).
[49] E. L. Knuth and U. Henne, J. Chem. Phys. **110**, 2664 (1999).
[50] W. T. Ashurst and B. L. Holian, J. Chem. Phys. **111**, 2842 (1999).
[51] D. E. Grady, J. Appl. Phys. **53**, 322 (1982).